Hydrogeology Journal
https://doi.org/10.1007/s10040-019-01934-z

PAPER

Using water temperature series and hydraulic heads to quantify hyporheic exchange in the riparian zone

Jie Ren[1] · Wenbing Zhang[1] · Jie Yang[1] · Yinjun Zhou[2]

Received: 8 September 2018 / Accepted: 21 January 2019

Abstract

Surface-water/groundwater exchange through the evaluation of riparian-zone temperature data has attracted increasing attention in recent years. The Fox Ditch Canal, Nevada, USA, was chosen for this study on seasonal variations of riparian-zone water exchange. Groundwater temperature and hydraulic head real-time monitoring data were collected from March to November 2012. A calibrated hydro-thermal coupling model was used to characterize the riparian-zone temporal and spatial temperature distribution, thereby providing a standard against which the performances of four analytical solution models for calculated riparian-zone vertical seepage velocity could be assessed. The results indicated that the proposed model provided a simulation that was able to represent dynamic changes in riparian-zone soil temperature. Although small variations in patterns and magnitudes of riparian-zone water exchange were evident at a daily scale, they varied significantly over a seasonal scale. Comparison of the results of the four analytical solutions and numerical computation found that the Hatch solution by the amplitude method provided the highest accuracy for calculating groundwater velocity in this area (2.47×10^{-6} to 3.15×10^{-6} m/s). Global sensitivity analysis of hydro-thermal coupling model parameters showed that porosity had the most significant impact on temperature in the model.

Keywords Hyporheic exchange · Riparian zone · Analytical solutions · Vertical seepage velocity · Groundwater/surface-water relations

Introduction

Surface-water/groundwater (SW–GW) exchange has been the focus of hydrology, hydrogeology, environmental sciences and water resources management; therefore, spatial-temporal variation of SW–GW exchange is of great significance (Kinal and Stoneman 2012; Chen et al. 2017; Saha et al. 2017; Ibrakhimov et al. 2018). Surface-water bodies such as rivers, brooks, lakes, wetlands, irrigation ditches and offshore seawater usually exchange with GW through the permeable geological strata separating them. Because there is always a concurrent transfer of energy during SW–GW exchange, temperature, as a reflection of the state of energy, can reflect spatial-temporal variation in hydraulic exchange and provides an easy-to-measure and pollution-free natural tracing method (Engelhardt et al. 2011, 2013). The observation of spatial-temporal differences in temperature at the bottoms of rivers, lakes, wetlands and irrigation canals provides a representation of GW movement, thereby providing a measure of exchange between GW and SW (Constantz 2008; Mutiti and Levy 2010; Munz et al. 2016; Wilson et al. 2016).

The hyporheic zone is the saturated sedimentary layers under a riverbed and in the riparian zone where there is exchange of SW and GW materials and energy, and is also an area containing its own niche biological community (Lemke et al. 2013; Liao et al. 2013). The region of SW–GW exchange through riparian zone sedimentary layers is known as the riparian hyporheic layer. The riparian hyporheic layer has received increasing attention in recent years (Hoang et al. 2017; Liu et al. 2018; O'Toole et al. 2018). The hyporheic exchange processes occurring in the riparian hyporheic layer, which is an important part of the

✉ Jie Ren
renjie@xaut.edu.cn

[1] State Key Laboratory of Eco-hydraulics in Northwest Arid Region of China, Xi'an University of Technology, Xi'an 710048, Shaanxi, China

[2] Changjiang River Scientific Research Institute, Wuhan 430010, China

Published online: 07 February 2019

hyporheic zone, regulates the exchanges of water, heat and other materials, thereby exerting a significant impact on GW quantity and quality (Edwardson et al. 2003). Vogt et al. (2012) stressed that infiltration of river water is important for the ecologies of both the hyporheic and riparian GW zones, and also supplies the GW used by humans through riverbank filtration. The use of heat as a tracer to estimate SW–GW exchange rates is impeded by the spatial and temporal variations in exchange fluxes; therefore, quantifying the spatial and temporal variations in seepage velocity is important.

Hyporheic exchange is affected by many factors. At the meander scale, various geomorphological characteristics including sinuosity, topography, bars, pool-riffle sequences and bed forms can influence hydrological and biogeochemical processes in the hyporheic zone (Boano et al. 2006; Cardenas 2007; Dwivedi et al. 2017, 2018a). The study of the hyporheic zone is now relatively mature, although most studies have focused on riverbed vertical hyporheic exchange (Lautz 2012; Fox et al. 2014, 2016; Hester et al. 2016; Huang and Chui 2018). Hyporheic exchange in fact occurs both in a vertical direction below the riverbed and in a lateral direction into the riparian zone floodplain (Dwivedi et al. 2018b), although they differ in terms of exchange mechanism, ecological process and material transport. Molina-Giraldo et al. (2011) simulated the coupling of the temperature-seepage field by establishing a two-dimensional (2-D) model of SW recharge to GW and found that temperature dispersion in the shallow aquifer of the riparian hyporheic layers was greatly influenced by heat transfer in the unsaturated zone. Vogt et al. (2012) monitored the temperature of shallow GW using a distributed optical fiber temperature (DTS), and through analyzing the temperature time series of the vertical section, identified an uneven spatial distribution of GW temperature in the riparian zone due to the impact of GW velocity at different depths. Kiel and Cardenas (2014) detected lateral hyporheic exchange throughout the Mississippi River network, and concluded that practically all water reaching the mouth had circulated through the lateral hyporheic zone. Arora et al. (2016) evaluated the cumulative impact of reduced GW and sediments along the riverbanks of the Colorado River and quantified the effects of water-table fluctuations and temperature gradients on subsurface carbon fluxes in the floodplain. Yabusaki et al. (2017) used saturated flow varying across three dimensions and biogeochemical reactive transport modeling to build a systematic and mechanistic understanding of the processes, properties and conditions controlling spatially and temporally variable biogeochemistry in a small semiarid floodplain.

The aforementioned large number of studies demonstrate the importance of lateral exchange in the riparian zone. However, few studies have focused on temporal and spatial heterogeneity of temperature in the riparian zone with the use of water temperature and hydraulic head data to describe lateral riparian SW–GW exchange (Engelhardt et al. 2013; Liu et al. 2018). Moreover, there have been few attempts to quantify the SW infiltration rate of the riparian zone by use of temperature, and most have concentrated on the riverbed (Rau et al. 2010; Yao et al. 2015; Lu et al. 2017; Wang et al. 2017a); therefore, further study of SW–GW exchange in the riparian zone based on temperature time series analytical solution models would be of value. In the current study, real-time GW temperature and hydraulic head data were used to establish a hydro-thermal coupling model based on COMSOL Multiphysics, which originated from the Fox irrigation canal in Mason Valley and was published by the US Geological Survey (USGS) at Reston, Virginia, USA. Seasonal variations in the riparian zone temperature were analyzed. The riparian zone GW velocity results of four typical analytical solution models within VFLUX 2 were compared based on temperature series data to verify the flow field characteristics of the riparian zone. The mathematical models of riparian zone GW flow and heat transfer contained a large number of parameters, which required extensive model calibration; therefore, a sensitivity analysis was required to identify the most important parameters. The Morris method was used to determine the main factors affecting the temperature of the riparian zone to reduce the workload required for model correction and to provide a reference for related studies.

Study site

Figure 1 shows the location of the study site canal, watershed and monitoring stations. The data used were from a field test performed by the USGS (Reston, VA) within the Walker River Basin from March to November, 2012 (Naranjo and Smith 2016). The field test aimed to determine irrigation canal seepage loss within basin. The Walker River is located in Nevada, with a drainage area of approximately 10,230 km^2 and a total length of 100 km. The East and West Walker rivers converge at Mason Valley and then flow into Walker Lake. Flow in the river mainly originates from the Sierra Nevada Mountain meltwaters and the river is the major source of water for irrigated agriculture in Nevada. The annual average temperature of the Walker River Basin ranges from −4 to 35 °C, with a maximum in July and minimum in December. Alfalfa is the dominant crop and the total irrigated area is 534,000 acres, covering regions such as the Bridgeport, Antelope, Smith and the Mason valleys in California and Nevada. Surface water is usually used for agricultural irrigation, with GW used as an alternative during drought years. The present study used data collected from monitoring station 2 of the Fox Ditch Canal at Mason Valley.

Researchers from the USGS placed water level and temperature sensors along the riverbed and riparian zone of the Fox Ditch Canal for real-time monitoring of water level and

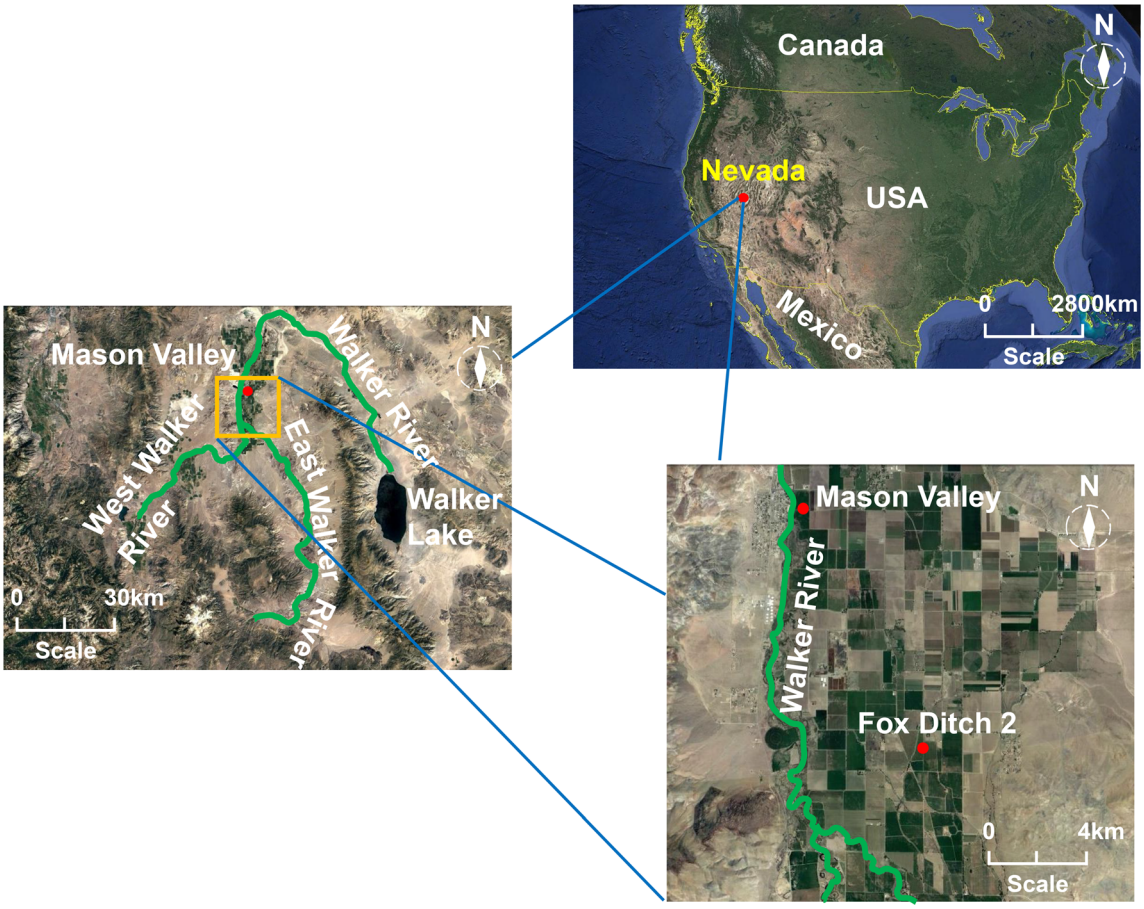

Fig. 1 Map showing the canal location, watershed and monitoring stations

water temperature. PVC temperature monitoring rods containing strainers were inserted into the sedimentary layers of the riparian zone. Temperature probes were then hung on the PVC rods 2.8 and 5.8 m away from the river center to measure water temperature at depths of 0.50, 0.70, 1.50 and 2.15 m, and 1.20, 1.70, 2.30 and 2.75 m, respectively. The water level and SW temperature of the riverbed were monitored using a Micro-Diver pressure sensor (accuracy: ±1.0 cm; resolution: 0.2 cm) and automatic temperature data recorder (accuracy: ±0.1 °C; resolution: 0.01 °C), both manufactured by Schlumberger. The riverbank surface soil temperature was monitored using an iBcod type-L temperature sensor (accuracy: ±0.5 °C; resolution: 0.5 °C) manufactured by Alpha Mach. The hydraulic heads and temperature data monitored during the test were recorded and stored by a data recorder every 1 h.

Numerical modeling

Model tools

The standard finite-element model COMSOL Multiphysics was used to simulate water flow and heat transport (Cardenas 2009; Sawyer et al. 2012; Munz et al. 2017). COMSOL Multiphysics is a numerical simulation software which simulates physical SW–GW exchange mechanisms based on the finite element method by solving a partial differential equation (single field) or partial differential equation groups (multi-field).

VFLUX 2 was used to calculate the seepage velocity of GW (Gordon et al. 2012), and is the first published computer program capable of calculating water flux from time series temperature data. The software allows completely automatic data pre-processing, including robust filtering with Dynamic Harmonic Regression (DHR), and is the first method to allow the use of a sliding window to identify changing flux rates with depth at a high spatial resolution (Irvine et al. 2015).

Flow model

The saturated-unsaturated seepage field can be expressed by the Richards equation (Richards 1931):

$$\rho_w\left(\frac{C_m}{\rho_w g}+S_e S_s\right)\frac{\partial p}{\partial t}+\nabla\rho_w\left(-\frac{K_s K_r(\theta)}{\mu(T)}\nabla(p+\rho_w g z)\right)=Q_m \quad (1)$$

where ρ_w is water density, C_m is water capacity, g is the acceleration of gravity, S_e is the relative saturation of soil, S_s is elastic water storage rate; p is the intensity of pressure, t is time, ∇ is a Laplace operator, θ is moisture content, K_s is hydraulic conductivity of saturated media, $K_r(\theta)$ is the relative hydraulic conductivity of the unsaturated zone ($0 \le K_r(\theta) \le 1$) (the function of moisture content θ), $\mu(T)$ is water dynamic viscosity, $\mu(T) = 0.00002414 \times 10^{(247.8/(T+133.16))}$ (Kipp 1987) and is a function of temperature, z is the elevation of calculated point position, and Q_m is the water source.

To date, some empirical formulae to represent of soil moisture characteristics of the unsaturated zone have been proposed. The most accepted include the models of van Genuchten (van Genuchten 1980), Brooks-Corey (Milly 1987) and Gardner (Milly 1987; Gardner et al. 1970). Among the proposed models, the van Genuchten model is characterized by a high accuracy (Shao and Horton 1998; Young et al. 2002), specific physical definitions of parameters, good applicability and a fitted curve capable of demonstrating the features of soil during the drying, transition and saturation periods; it is widely applied in the calculation of unsaturated soil (nearly all soil types). The van Genuchten model can be written as:

$$\theta = \theta_r + S_e(\theta_s - \theta_r) \tag{2}$$

where S_e is the relative saturation of soil, θ_r is residual moisture content and θ_s is saturated moisture content. The formula for the relative saturation of soil is:

$$S_e = \frac{1}{\left[1 + (\alpha h_p)^{n_v}\right]^m} \tag{3}$$

where h_p is the pressure head ($h_p = p_w/\rho_w g$) which is equal to the suction head h_c in the unsaturated zone, α is the reciprocal of the air entry value of the soil moisture characteristic curve, n_v is the parameter indicative of the gradient of the soil moisture characteristic curve and $m = 1 - 1/n_v$. The empirical formulae used to calculate the water capacity of soil C_m and the relative hydraulic conductivity $K_r(\theta)$ in the unsaturated zone respectively are:

$$C_m = \frac{\alpha m}{1-m}(\theta_s - \theta_r) S_e^{\frac{1}{m}} \left(1 - S_e^{\frac{1}{m}}\right)^m \tag{4}$$

$$K_r(\theta) = S_e^{\frac{1}{2}} \left[1 - \left(1 - S_e^{\frac{1}{m}}\right)^m\right]^2 \tag{5}$$

Heat transport model

The saturated-unsaturated heat transfer model can be expressed by the following equation (Healy and Ronan 1996):

$$\frac{\partial\left(\rho_{eq} C_{eq} T\right)}{\partial t} = \nabla\left(\lambda_{eq} \nabla T\right) + \nabla(\theta \rho_w C_w \mathbf{D_H} \nabla T) - \nabla(\theta \rho_w C_w \mathbf{u} T) + Q_s \tag{6}$$

where ρ_{eq} is equivalent density, C_{eq} is equivalent specific heat capacity, T is water temperature, t is time, ∇ is a Laplace operator, λ_{eq} is equivalent thermal conductivity, θ is moisture content which is equal to porosity in the saturated zone, ρ_w is water density, C_w is the specific heat capacity of water, $\mathbf{D_H}$ is the hydrodynamic dispersion coefficient, $\mathbf{u}$ is mean water velocity calculated by $\mathbf{u} = \mathbf{v}/\theta$ ($\mathbf{v}$ is the Darcy seepage velocity) and Q_s is the heat source.

The coefficient of hydrodynamic dispersion is a parameter representing the ability of porous media to diffuse a contaminant at a certain flow velocity.

$$\mathbf{D_H}_{ij} = \alpha_T |v| \delta_{ij} + (\alpha_L - \alpha_T) \mathbf{v}_i \mathbf{v}_j |v| \tag{7}$$

where α_T is transverse dispersion, $|v|$ is the magnitude of flow velocity vector, δ_{ij} is a kriging constant equal to 1 when $i = j$ and otherwise 0, α_L is longitudinal dispersion, $\mathbf{v}_i$ is the vector of flow velocity in direction i and $\mathbf{v}_j$ is the vector of flow velocity in direction j.

The equivalent density and equivalent specific heat capacity of soil follow the volume averaging law and respectively are:

$$\rho_{eq} = (1-n)\rho_s + \theta \rho_w + (n-\theta)\rho_g \tag{8}$$

$$C_{eq} = (1-n)C_s + \theta C_w + (n-\theta)C_g \tag{9}$$

where ρ_s, ρ_w and ρ_g represent the density of soil, water and air, respectively, and n is the porosity of the porous medium. Under saturated conditions, $\theta = n$, and Eq. (6) is the convection current heat transport equation in a saturated aquifer. C_s and C_g represent the specific heat capacities of soil and air, respectively.

Analytical methods in VFLUX 2

The temperatures of the shallow geological layers fluctuate periodically due to the influence of atmospheric temperature. The fluctuation attenuates with increasing depth increases and this is closely related to the movement of GW (Lee et al. 2013). Thus, the present study proposed an analytical method to calculate GW velocity in the vertical direction using time series temperature data. Four typical analytical solution models are provided by Hatch (Hatch et al. 2006), Keery (Keery et al. 2007), McCallum (McCallum et al. 2012) and Luce (Luce et al. 2013), with all assuming that SW temperature at the upper boundary follows a sinusoidal fluctuation—$T(z, t) = T_w(t)$ at $z = 0$; $T_w(t)$ is a set of SW temperatures which were described as the superposition of trigonometric functions. The lower boundary is a homogeneous isotropic half-

infinite space, and the infinity is the crustal constant temperature layer—$T(z, t) = T_A$ at $z = \infty$; T_A is the average ambient temperature. The initial boundary condition is $T(z, t = 0)$ (Stallman 1965; Goto et al. 2005; Schornberg et al. 2010). More details of the four analytical solution models are provided in Appendix 1.

Based on the preceding four analytical solution models, the VFLUX 2 calculation program was used to calculate vertical seepage velocity. Since the analytical solution models used are suitable for homogeneous porous media, it was assumed that they conformed to this condition. Parameters required for the calculation, including effective thermal conductivity, thermal dispersion coefficient, specific heat capacities of water and soil, and the porosity of saturated layers in the riparian zone, were determined according to the test performed by Naranjo and Smith (2016). The parameters used in the VFLUX 2 calculation are listed in Table 1.

Data processing

The present study used an analytical model with input requirements of diurnal temperature data as these data have a large amplitude and are easy to observe. The measured temperature time series data contained multi-periodic-superposed signals, and were therefore filtered to obtain sinusoidal signals of diurnal temperature fluctuation for application to the Hatch and Keery analytical solution models. The present study used dynamic harmonic regression analysis (DHR) which is suitable for processing periodic signals to filter the measured data.

The measured temperature data were filtered through the DHR method with the fundamental frequency set at $P = 12$ h. The temperature series data which fluctuated in accordance with a sinusoidal harmonic wave were then obtained (Fig. 2). The results of DHR analysis showed a good fit to measured data. Several mutation points were present on the curves of the aperiodic factors, indicating that temperature was not stable.

Model setup

Using the aforementioned numerical models, COMSOL Multiphysics was able to identify finite element solutions to saturated-unsaturated seepage and the temperature coupling model through modifying relevant modules. According to the difference in soil permeability, the soil types in the solution zone could be categorized into zones 1 and 2 (Fig. 3). No-flow boundaries were set on the left and right sides of the saturated-unsaturated seepage field, and the permeable boundary was set at the bottom. The variable head boundary was set at the river-water-contact interface, which was imposed on the boundary by defining a cubic spline interpolation function in COMSOL Multiphysics. The initial hydraulic head was set according to the value measured by the water level sensor. Adiabatic boundaries were set on the left and right sides as well as at the bottom of the temperature field. The air temperature boundary was set at the air contact interface. The water temperature boundary was set at the river-water-contact interface. The initial temperature was set according to the mean of preliminary sensor measurements. The initial temperatures of zones 1 and 2 were 6 and 5 °C, respectively. Figure 4 shows the change in hydraulic head from March 26, 2012 to November 4, 2012. The hydraulic and temperature parameters used in the calculation model are listed in Table 2.

Table 1 Parameters of the VFLUX 2 calculation

Porosity (−)	Thermal dispersion coefficient (1/m)	Thermal conductivity [cal·(s·cm·°C)$^{-1}$]	Heat capacity of water [kcal·(kg·°C)$^{-1}$]	Heat capacity of soil [kcal·(kg·°C)$^{-1}$]
0.41	0.010	0.000239	1.000	0.262

Model evaluation

The simulation accuracy of the proposed model was evaluated using the root mean square error (RMSE), Pearson correlation coefficient (PCC) and Nash-Sutcliffe model efficiency coefficient (NSE) (Tao et al. 2013; Liu et al. 2016):

$$\mathrm{RMSE} = \sqrt{\frac{1}{m}\sum_{i=1}^{m}\left(T_{\mathrm{obs},i} - T_{\mathrm{model},i}\right)^2} \tag{10}$$

$$\mathrm{PCC} = \frac{\sum_{i=1}^{m}\left(T_{\mathrm{obs},i} - \overline{T}_{\mathrm{obs},i}\right)\left(T_{\mathrm{model},i} - \overline{T}_{\mathrm{model},i}\right)}{\sqrt{\sum_{i=1}^{m}\left(T_{\mathrm{obs},i} - \overline{T}_{\mathrm{obs},i}\right)^2}\sqrt{\sum_{i=1}^{m}\left(T_{\mathrm{model},i} - \overline{T}_{\mathrm{model},i}\right)^2}} \tag{11}$$

$$\mathrm{NSE} = 1 - \frac{\sum_{i=1}^{m}\left(T_{\mathrm{obs},i} - T_{\mathrm{model},i}\right)^2}{\sum_{i=1}^{m}\left(T_{\mathrm{obs},i} - T_{\mathrm{obs},i}\right)^2} \tag{12}$$

where m is the number of data, $T_{\mathrm{obs},i}$ and $T_{\mathrm{model},i}$ are the experimental temperature and the simulated temperature at moment i, respectively, and $\overline{T}_{\mathrm{obs}}$ and $\overline{T}_{\mathrm{model}}$ are the average experimental temperature and the average simulated temperature, respectively. RMSE ranges from 0 to $+\infty$, with a smaller value indicating less deviation between the simulated and experimental values. The PCC ranges between −1 and 1, with a larger absolute value indicating a stronger correlation. The closer the correlation coefficient to 1 or −1, the stronger the correlation, and the closer to 0, the weaker the correlation. In general, values of 0.8–1.0, 0.6–0.8 and 0.4–0.6 represent extremely strong, strong and moderate correlations. The NSE, which ranges from $-\infty$ to 1, can be used as a criterion to assess the predictive power of a model, with a value closer to 1.0 indicating less deviation between the measured and simulated

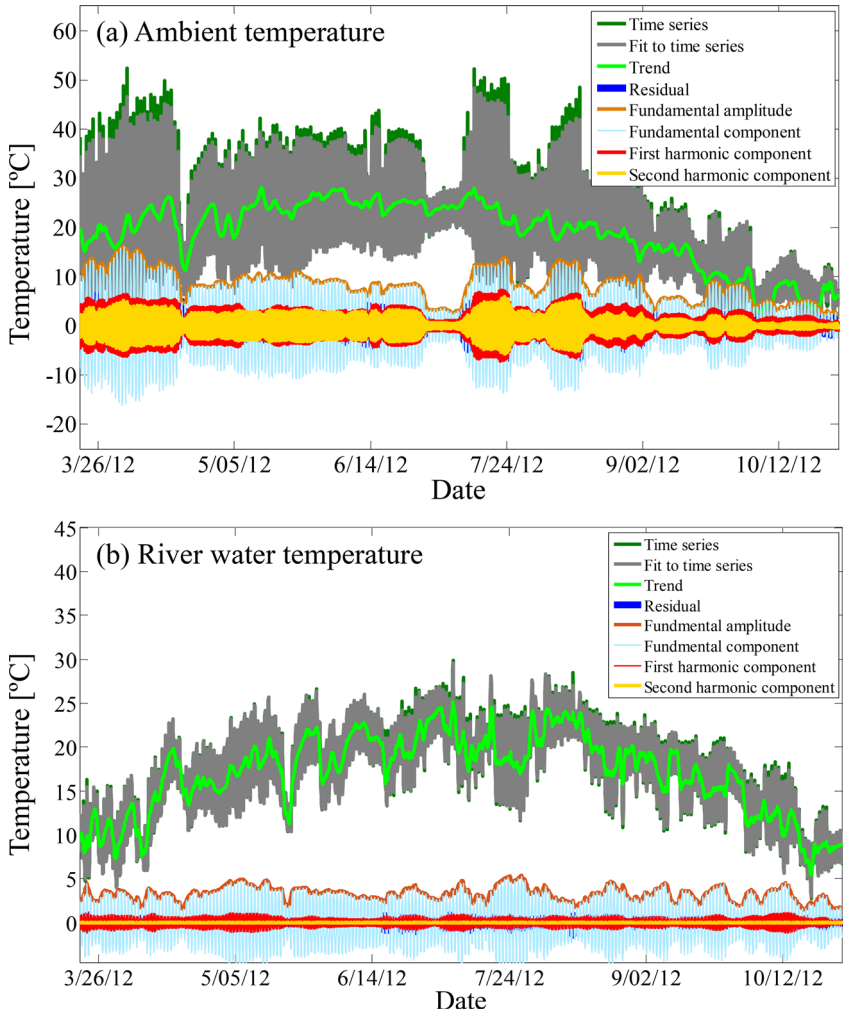

Fig. 2 Dynamic Harmonic Regression (DHR) filter analysis results for the temperature-time-series data: **a** ambient temperature; **b** river-water temperature

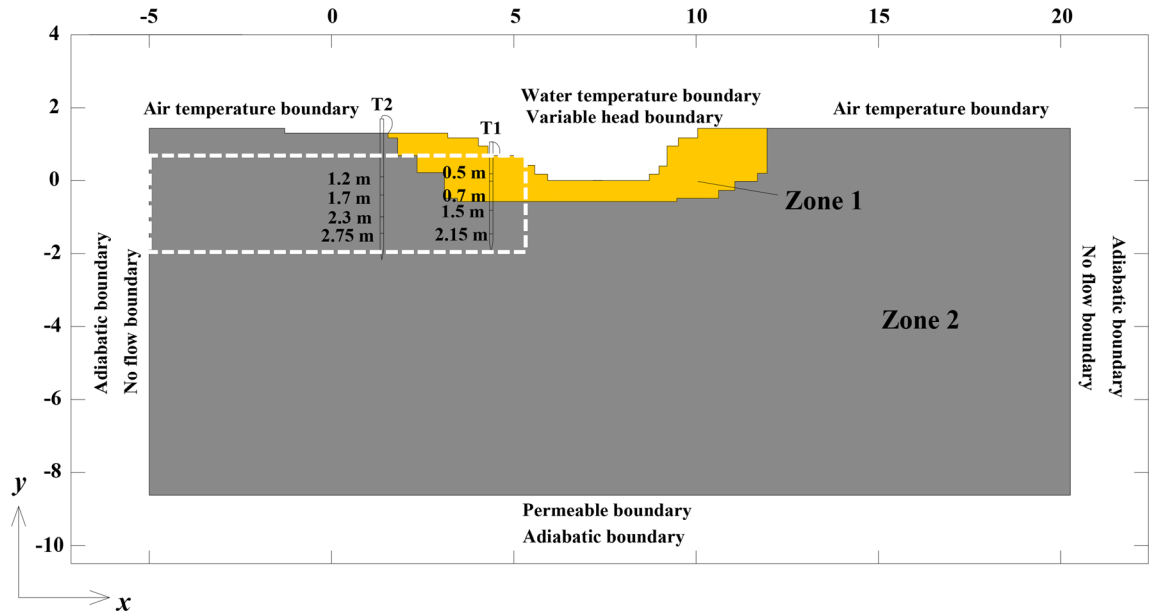

Fig. 3 Flow domain and boundary conditions used in the COMSOL Multiphysics simulations (unit: m)

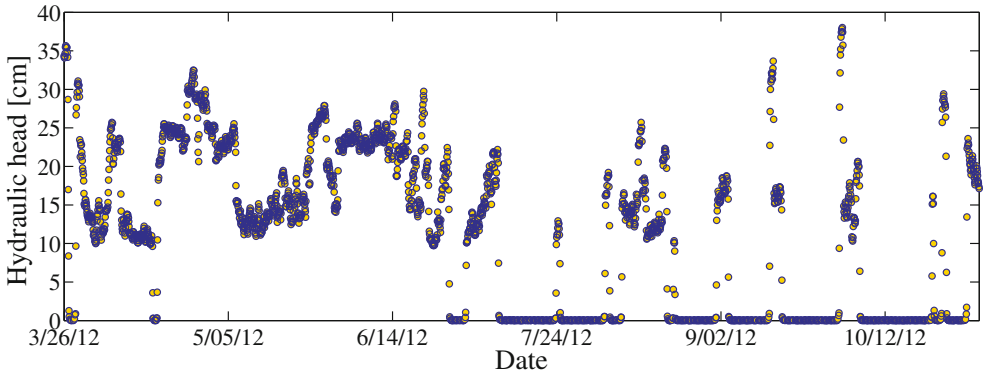

Fig. 4 The changes in hydraulic head of the river from March 26, 2012 to November 4, 2012

value, and NSE > 0.6, close to 0 and < 0 representing approximate accordance, basically reliability and unreliability of the model, respectively.

Sensitivity analysis

Many uncertainties exist in the riparian hydro-thermal coupling model, including the many parameters, scale diversification of model parameters and manufacturing errors, thereby increasing the uncertainty of model prediction. An uncertainty and sensitivity analyses of model parameters can effectively identify the effect of individual parameters on the output variables and the interactions between model parameters and results (Sobol 1993). Sensitivity analysis was used to identify the main factors responsible for temperature variation, thereby allowing the

Table 2 Hydraulic and thermal parameters for calibrating and evaluating the hydro-thermal coupling model

Parameter	Symbol	Zone	Value	Units	Source
Hydraulic parameters					
Horizontal hydraulic conductivity	K_h	1	0.010	m/h	Naranjo and Smith (2016)
		2	1.52		
Vertical hydraulic conductivity	K_v	1	0.010	m/h	Naranjo and Smith (2016)
		2	0.15		
Porosity	n	1	0.41	–	Naranjo and Smith (2016)
		2	0.41		
Saturated moisture content	θ_s	1	0.43	m^3/m^3	Calibration
		2	0.43		
Residual moisture content	θ_r	1	0.057	m^3/m^3	Naranjo and Smith (2016)
		2	0.057		
van Genuchten parameters	α	1	12.4	m^{-1}	Naranjo and Smith (2016)
		2	12.4		
	n_v	1	2.28	–	Naranjo and Smith (2016)
		2	2.28		
Thermal parameters					
Heat capacity of solids	C_s	1	1.1×10^6	$J/(m^3 \cdot °C)$	Naranjo and Smith (2016)
		2	1.1×10^6		
Thermal conductivity of solids	λ_s	1	360	$J/(h \cdot m \cdot °C)$	Naranjo and Smith (2016)
		2	360		
Heat capacity of water	C_w	1	4.2×10^6	$J/(m^3 \cdot °C)$	Naranjo and Smith (2016)
		2			
Longitudinal dispersion	α_L	1	0.01	m	Naranjo and Smith (2016)
		2	0.01		
Transverse dispersion	α_T	1	0.01	m	Naranjo and Smith (2016)
		2	0.01		
Thermal conductivity of water	λ_w	1	2088	$J/(h \cdot m \cdot °C)$	Naranjo and Smith (2016)
		2	2088		

study to concentrate on improving the accuracy of observation of these identified factors, and even if minor factors were neglected, a numerical model could be obtained that provided a close approximation of reality.

Temperature of the riparian zone is under the combined influence of regional heat condition and seepage field. If it is assumed that the calculation area is fairly large, it can also be assumed that no heat exchange between the seepage system in the riparian zone and the geological body occurs (Gerecht et al. 2011). The impacts of seepage media on temperature can be reflected through basic variables such as hydraulic conductivity, specific heat capacity, porosity and thermal conductivity. Therefore, the present study included the influences of thermal conductivity (λ_s), specific heat capacity of soil (C_s), saturated moisture content (θ_s), residual moisture content (θ_r), horizontal hydraulic conductivity (K_h), vertical hydraulic conductivity (K_v) and porosity (n). The initial values for the factors used in the global sensitivity analysis are shown in the Table 3.

A global sensitivity analysis is able to identify the interactions between parameters and to determine the effect of multiple parameters on the response variable (Wang et al. 2017b). These global sensitivity analysis methods include multivariate regression (Mckay et al. 1979), the Sobol sensitivity test method (Sobol 1993), the Fourier amplitude sensitivity test (FAST) (Cukier et al. 1973) and the Morris method (Morris 1991). When compared with other global sensitivity analysis methods, the Morris method is able to analyze the influence of each parameter variation as well as the influence of interactions between multiple parameters on the model output (Campolongo et al. 1999). More detail on the Morris sensitivity analysis method is given in Appendix 2.

The evaluation indicators must be normalized as their units differ; thus, the indicators were represented as percentages indicating the ratio of the difference between the changed value and initial value to the initial value. The longitudinal section was used as the research object due to the spatial characteristics of the numerical model. The distributions of temperature after changing parameters were obtained through numerical simulation. The temperature variations were then represented as the difference between temperature after the parameter change and the benchmark temperature at each measuring point. The experimental period was set at to March 26, 2012 to April 11, 2012.

Results

Model calibration

Figure 5 shows the variation between COMSOL Multiphysics simulated temperature and measured values. The temperature data were collected from the eight monitoring points from temperature monitoring rods T1 and T2 in the riparian zone from March 26, 2012 to November 4, 2012. Table 4 shows the ranges of RMSE, PCC, and NSE at 1.14–2.78, 0.84–0.99 and 0.61–0.96, respectively, indicating simulated data were good representation of measured data.

Figure 5a shows that measured GW temperatures followed SW temperatures closely up to vertical (depth) and horizontal distances of 0.5 and 2.8 m (T1), respectively. The amplitude of diurnal SW temperature oscillations were not fully represented in GW at depths between 0.5 and 2.15 m. Similarly, measured temperature data collected 5.8 m from the riverbed center in a horizontal plane in the riparian zone (T2) showed slight diurnal temperature variations up to a depth of 1.2 m (Fig. 5b). Diurnal river-water temperature oscillations dissipated at a depth >1.70 m, and only longer-term temperature trends were reflected in GW.

Sensitivity of hydro-thermal coupling model parameters in the riparian zone

The Morris method for global sensitivity analysis assumed an increase in the parameter value by 10% to obtain both a reliable analysis result and a simplified calculation (Ren et al. 2018). Parameter combinations of each row of Matrix **B** were substituted into the coupling model of temperature to sequentially calculate the differences between simulated results, thereby identify the sensitivities of different parameter combinations. The global sensitivities of 28 different groups obtained by the Morris method are listed in Table 5. The bar graph in Fig. 6 illustrates the temperature variations (%) of different groups more directly.

Groups 1–7 illustrates that temperature variation resulted from only one parameter, with the order of influence of the different parameters being porosity (n) > vertical hydraulic conductivity (K_v) > residual moisture content (θ_r) > horizontal hydraulic conductivity (K_h) > saturated moisture content (θ_s) > thermal conductivity of soil (λ_s) > specific heat capacity of soil (C_s).

Table 3 The initial values for the factors used in the global sensitivity analysis

Zone	λ_s [J/(h·m·°C)]	C_s [J/(m^3·°C)]	θ_s (m^3/m^3)	θ_r (m^3/m^3)	K_h (m/h)	K_v (m/h)	n (–)
1	360	1.1×10^{-6}	0.43	0.057	0.010	0.010	0.41
2	360	1.1×10^{-6}	0.43	0.57	1.520	0.150	0.41

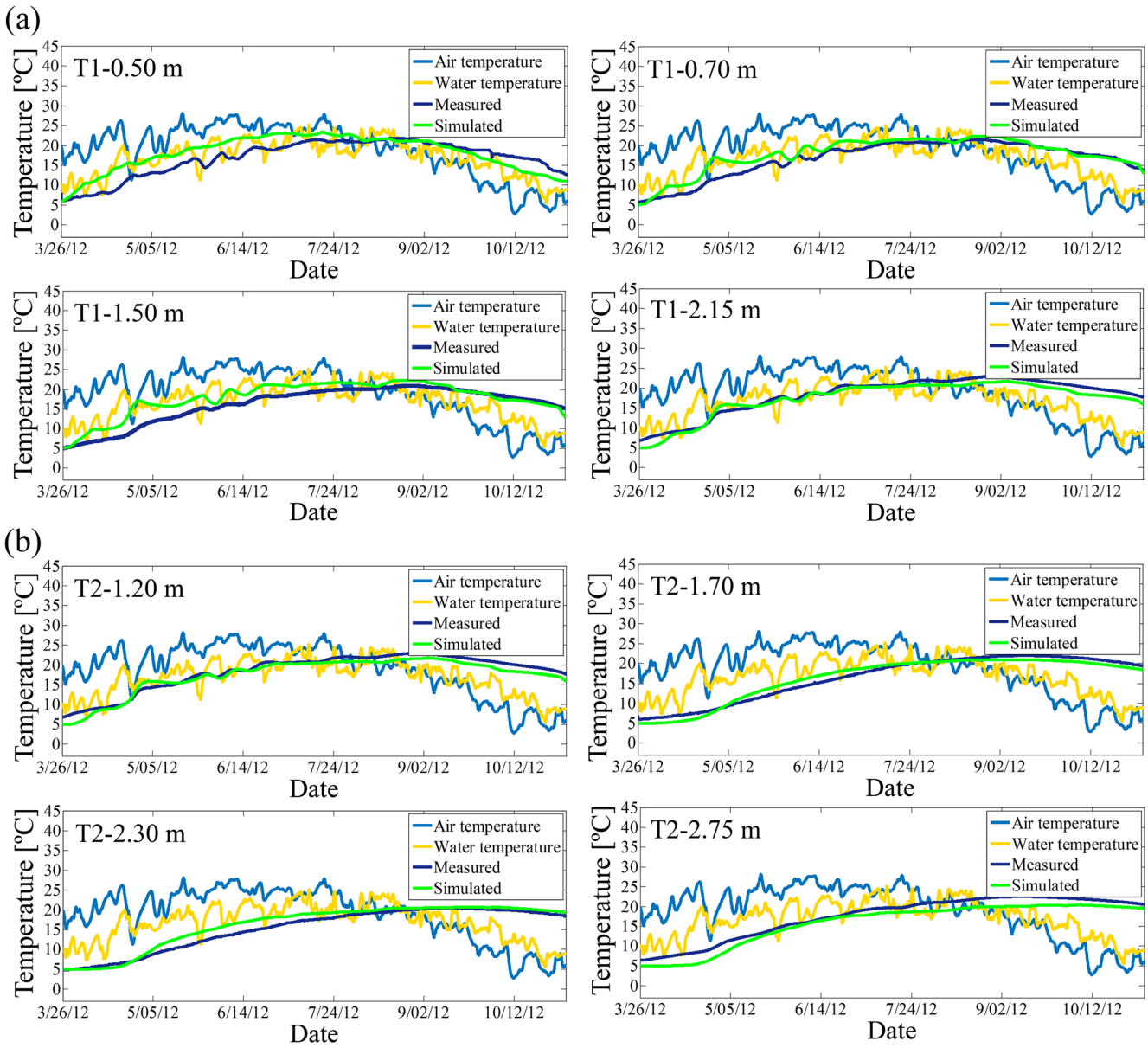

Fig. 5 Measured air and surface-water temperature, multilevel temperature data sets, and simulated temperature profiles (blue lines are measured data, green lines are model results): **a** T1 (2.8 m horizontally from the river center) and **b** T2 (5.8 m horizontally from the river center)

Table 4 The root mean square error (RMSE), Pearson correlation coefficient (PCC) and Nash-Sutcliffe model efficiency coefficient (NSE) for the simulated results of the calibrated model

Temperature sensor		RMSE (°C)	PCC	NSE
T1	0.50 m	2.78	0.84	0.61
	0.70 m	1.74	0.96	0.85
	1.50 m	2.36	0.93	0.73
	2.15 m	1.16	0.98	0.93
T2	1.20 m	1.29	0.97	0.94
	1.70 m	1.14	0.98	0.96
	2.30 m	1.39	0.98	0.93
	2.75 m	1.79	0.99	0.88

Groups 10, 12, 15, 17, 19, 25, 26 and 27 were identified as parameter combinations resulting in large temperature variations. These parameter combinations all included n, K_v, θ_r and K_h. indicating that these parameters remain the major factors influencing temperature in the riparian zone after considering interactions among parameters. More specifically, the extent of influence of the eight aforementioned groups on temperature differed, indicating that interactions between parameters within their impact on temperature.

The temperature variation resulting from group 28 in which all parameters were increased by 10% was lower than those of groups 10, 12, 15, 17, 19, 25, 26 and 27. It is known from groups 1–7 that the correlation between parameters and temperature in the riparian zone can be both negative and positive;

Table 5 Temperature variation based on analysis method for global sensitivity

Group	Parameter combination	Temperature variation (%)	Group	Parameter combination	Temperature variation (%)
1	λ_s	0.99	15	C_s, θ_s, θ_r	−3.95
2	C_s	−0.17	16	θ_s, θ_r, K_h	−1.71
3	θ_s	−1.20	17	θ_r, K_h, K_v	2.91
4	θ_r	−2.75	18	K_h, K_v, n	1.28
5	K_h	2.07	19	λ_s, C_s, θ_s, θ_r	−2.96
6	K_v	3.59	20	C_s, θ_s, θ_r, K_h	−1.88
7	n	−4.38	21	θ_s, θ_r, K_h, K_v	1.88
8	λ_s, C_s	0.82	22	θ_r, K_h, K_v, n	−1.47
9	C_s, θ_s	−1.20	23	λ_s, C_s, θ_s, θ_r, K_h	−0.89
10	θ_s, θ_r	−3.78	24	C_s, θ_s, θ_r, K_h, K_v	1.71
11	θ_r, K_h	−0.68	25	θ_s, θ_r, K_h, K_v, n	−2.50
12	K_h, K_v	5.66	26	λ_s, C_s, θ_s, θ_r, K_h, K_v	2.70
13	K_v, n	−0.79	27	C_s, θ_s, θ_r, K_h, K_v, n	−2.67
14	λ_s, C_s, θ_s	−0.21	28	λ_s, C_s, θ_s, θ_r, K_h, K_v, n	−1.68

thus, it is believed that this phenomenon results from interactions among different parameters.

Distribution of temperature in the riparian zones

A comparative analysis of diurnal temperature change in the riparian zone was conducted by analyzing temperatures at 12:00 am, 8:00 am, 1:00 pm and 8:00 pm on April 3, 2012, July 3, 2012 and November 3, 2012 (Fig. 7). All monitoring points on the temperature monitoring rods T1 and T2 were included to ensure direct observation of the change temperature in the riparian zone, and the study area are limited to within $-5.177\ \text{m} \le x \le 5.133\ \text{m}$ and $-2\ \text{m} \le y \le 0.686\ \text{m}$ within the area indicated by the white dotted lines in Fig. 3. The white curve in Fig. 7 represents the current level of GW; it is an unsaturated zone above the curve and saturated zone beneath the curve. Moreover, riparian zone temperatures could be categorized into three areas: high temperature ($T \ge 12.5$ °C), intermediate temperature (8.5 °C $\le T <$ 12.5 °C) and low temperature (4.5 °C $\le T <$ 8.5 °C). The size variations of the high,

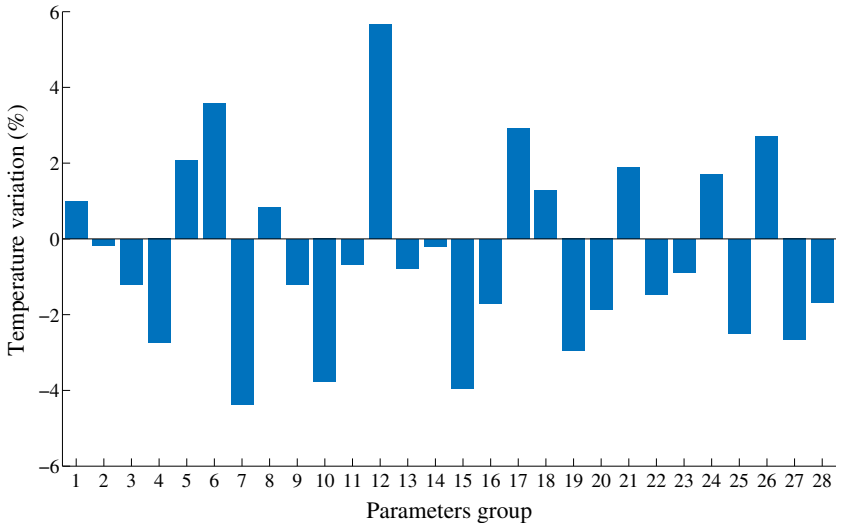

Fig. 6 Temperature variation based on global sensitivity analysis method. (group 1: λ_s; group 2: C_s; group 3: θ_s; group 4: θ_r; group 5: K_h; group6: K_v; group 7: n; group 8: λ_s, C_s; group 9: C_s, θ_s; group 10: θ_s, θ_r; group 11: θ_r, K_h; group 12: K_h, K_v; group 13: K_v, n; group 14: λ_s, C_s, θ_s; group 15: C_s, θ_s, θ_r; group 16: θ_s, θ_r, K_h; group 17: θ_r, K_h, K_v; group 18: K_h, K_v, n; group 19: λ_s, C_s, θ_s, θ_r; group 20: C_s, θ_s, θ_r, K_h; group 21: θ_s, θ_r, K_h, K_v; group 22: θ_r, K_h, K_v, n; group 23: λ_s, C_s, θ_s, θ_r, K_h; group 24: C_s, θ_s, θ_r, K_h, K_v; group 25: θ_s, θ_r, K_h, K_v, n; group 26: λ_s, C_s, θ_s, θ_r, K_h, K_v; group 27: C_s, θ_s, θ_r, K_h, K_v, n; group 28: λ_s, C_s, θ_s, θ_r, K_h, K_v, n)

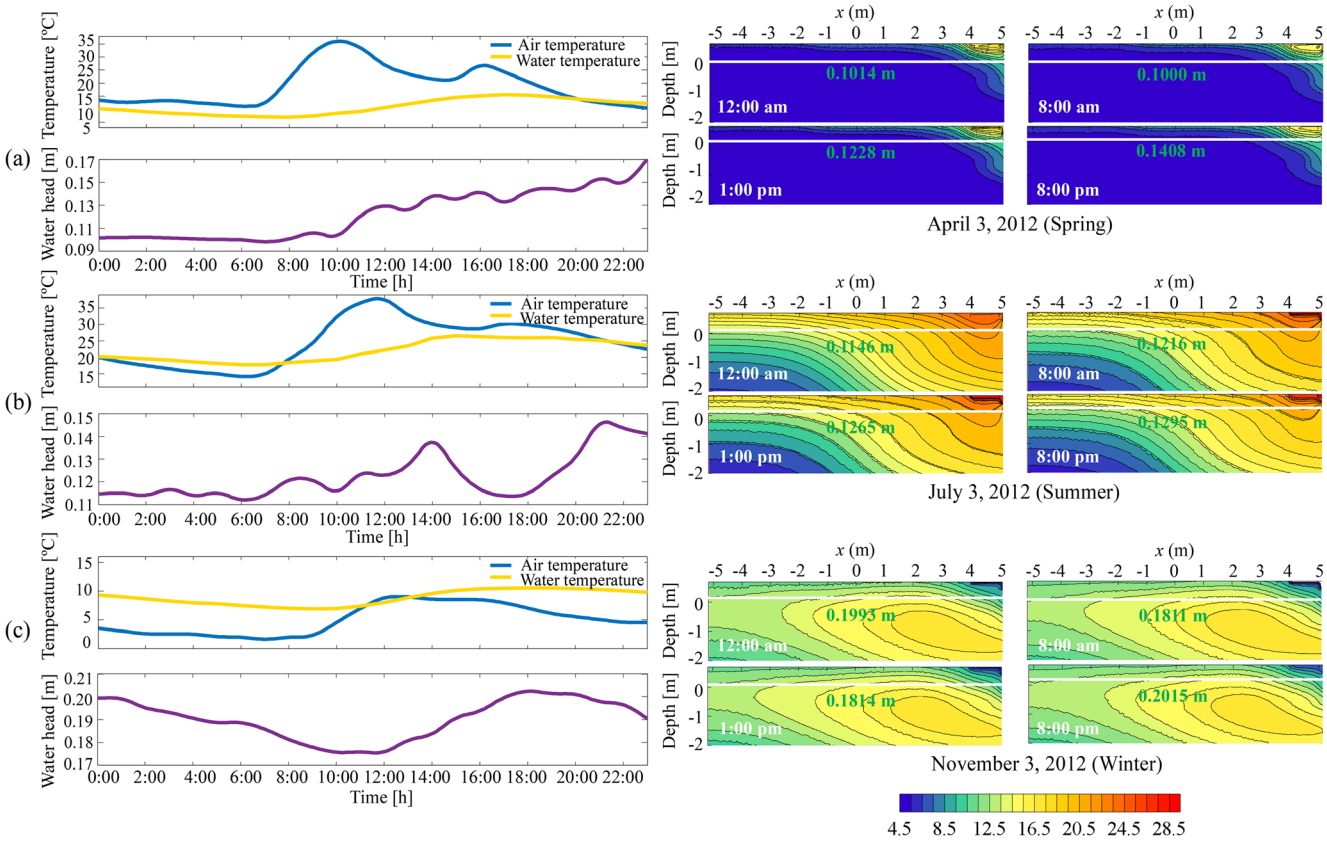

Fig. 7 Distribution of temperature across different seasons in riparian zone. **a** April 3, 2012; **b** July 3, 2012; **c** November 3, 2012. The blue and yellow curves on the left-hand side of the figure indicate the change in air and water temperature at different times in a day. The purple curve indicates the change in the head of the day at the corresponding moment. The right-hand side of the figure is the corresponding temperature distribution at the three different dates, at times 12:00 am, 8:00 am, 1:00 pm and 8:00 pm. The white curve represents the groundwater level and the green number indicates the groundwater level at the current time

intermediate and low temperature areas clearly indicated the extent to which the three time points vary (see Table 6). It can be seen from Fig. 7 that:

1. During spring (Fig. 7a), the lateral riparian zone can be divided into a high-temperature, intermediate-temperature and low-temperature region, with temperature decreasing with further distance away from the riverbank. The observation on April 3, 2012 from 12:00 am and 8:00 am showed an expansion of the high-temperature regions of the unsaturated and saturated zones concurrent with the rise in ambient and river water temperature; yet the temperature of the low-temperature regions decreased. At 1:00 pm, the temperature of the high-temperature region of the saturated zone nearby the riverbank increased and that of the high-temperature region of the unsaturated zone nearby the riverbank increased. At 8:00 pm, despite a decline in ambient and river water temperatures, the

Table 6 The size of high-, intermediate- and low-temperature regions in the study area at different times (units: m^2)

Regions by temperature	April 3, 2012 (spring)				July 3, 2012 (summer)				November 3, 2012 (winter)			
	12:00 am	8:00 am	1:00 pm	8:00 pm	12:00 am	8:00 am	1:00 pm	8:00 pm	12:00 am	8:00 am	1:00 pm	8:00 pm
High temperature ($T \geq 12.5$ °C)	0.413	0.424	0.430	0.424	18.577	17.394	17.546	18.143	20.038	20.057	20.057	20.557
Intermediate temperature ($8.5 \leq T < 12.5$ °C)	0.685	0.751	0.760	0.825	5.875	5.594	6.199	5.277	6.560	7.346	6.433	6.689
Low temperature ($4.5 \leq T < 8.5$ °C)	26.595	26.518	26.503	26.444	3.241	4.701	3.948	4.273	0.152	0.309	1.203	0.477

high-temperature zone expanded and the low-temperature zone shrunk due to the increased level of river water.

2. During summer (Fig. 7b), temperature stratification was more obvious than during spring (Fig. 7a). With the change in season, increasing air temperature resulted in increasing SW temperature. Figure 7a,b illustrates a lag in SW temperature response to increasing air temperature and larger fluctuation in water level in spring than in summer, with increasing water level with increasing temperature. Surveys by Naranjo and Smith (2016) indicated that this is due to acceleration of snow melt. In conclusion, the low temperature area was mainly concentrated in the saturated zone far from the river, with higher temperatures for the offshore area and temperature being inversely proportional to distance offshore. The observations of temperature on July 3, 2012 found that between 12:00 am and 8:00 am, the rise in air temperature resulted in a high temperature of the unsaturated zone nearby the river; hysteresis effects were evident, with SW temperature dropping gradually during this period, and the temperature of the low-temperature region of the saturated zone far away from the river increasing. At 1:00 pm, both the ambient and SW temperatures were high and the river water level was rising. Consequently, there was an expansion of the high-temperature regions of both the saturated and unsaturated zones nearby the river; yet, the low-temperature region of the saturated zone shrunk. At 8:00 pm, with a gradual drop in both ambient temperature and SW temperature, an increase and decrease of the low-temperature and high-temperature regions were evident, respectively.
3. The air temperature in winter (Fig. 7c) was significantly lower than in spring and summer, directly resulting in decreases to SW temperature of the unsaturated zone and shrinking of the high temperature area. Due to the increasing of water head in winter, a rise in GW level was evident with an increase and decrease in the saturated and unsaturated zones, respectively. Temperature stratification during winter was not obvious relative to that in summer. The lateral riparian zone can be roughly categorized into a high-temperature, intermediate-temperature and low-temperature region, with the low and intermediate temperature regions mainly situated in the unsaturated zone nearby the river and the saturated zone far from the river. Temperature observations on November 3, 2012 found that between 12:00 am and 8:00 am, declines in both ambient and SW temperature were evident along with a drop in river water level, and an expansion and retraction of the low-temperature and high-temperature regions, respectively. At 1: 00 pm, the laws of temperature distribution between the unsaturated and saturated zones were approximately consistent, with generally little variation. At 8:00 pm, the soil temperature of the unsaturated zone near the GW level was higher than those measured during the three previous times, indicating that GW temperature influenced the temperature of the unsaturated zone through heat conduction.

The unsaturated and saturated zones differed in spatial distribution of temperature both in summer and winter. The temperature of the unsaturated zone was higher than that of GW in summer, resulting in thermal stratification with higher temperature at the top. However, GW temperature was much higher than that of the unsaturated zone in winter, resulting in thermal stratification with a higher temperature at the bottom.

Table 6 shows little diurnal variation in the temperature of the riparian zone, indicating that the diurnal patterns and magnitudes of water exchange varied little. In contrast, the seasonal variations in temperature and water level had a relatively large impact on riparian zone temperature. From spring to summer, the increment of riparian high-temperature area accounted for 63.17% of total area, whereas the low-temperature decreased by 81.16%, indicating that the patterns and magnitudes of water exchange in the hyporheic zone varied significantly over the seasons. However, relatively weak variations in temperature were evident from summer to winter, with the increment of riparian high-temperature area accounting for 8.17% of the total area, and the low-temperature area decreasing by 12.66%, indicating that the degree of change of hyporheic exchange is also different during different seasons.

Comparison of analytical solutions for vertical seepage velocity derived from temperature time series

Data deflecting diurnal temperature fluctuation was critical to the precision of model. The extraction of effective sinusoidal signals within the temperature data using an appropriate filtering method was important. In most cases, mutation points were identified on the temperature time series curve which were generally the result of changes to the hydrodynamic condition or SW temperature and may have result in distortion of simulated results during filtering.

In theory, the measured temperature data of any two points on the vertical section could be used to calculate average GW velocity between the two points. However, it should be noted that the large distance between the two measuring points together with low GW flow velocity reduced the accuracy of the model due to the small amplitude ratio and large phase lag. Therefore, the GW velocity in the study area required estimation to establish an appropriate measuring point distance. The burial depth of the measuring point should not be large if the GW velocity is calculated using the diurnal temperature because the diurnal fluctuation cannot be monitored in deeper

geological layers. In addition, the amplitude method and phase method in VFLUX 2 for calculating the GW velocity must be based on homogeneous media. For these two reasons, temperature data collected at the measuring points set at 1.70 and 2.75 m on T2 were used for analysis.

Similarly, data collected from the two measuring at 1.70 and 2.75 m were filtered through DHR (see section 'Data processing') with the fundamental frequency set at $P = 12$ h, allowing the temperature series fluctuating in the sinusoidal harmonic wave to be obtained. This approach was taken, as oversampling the original data posed no disadvantage provided the data were resampled prior to DHR analysis. An oversample is better able to describe the diurnal signal in relation to high-frequency noise, which is then removed by the low-pass filter. When analyzing the temperature time series data, VFLUX used an integer resample factor (rfactor) of 12 for a reduced sampling rate of 12 samples per day (Gordon et al. 2012). The numerical method was used to extract the amplitude of temperature fluctuation after filtering. The amplitude ratio A_r is the ratio of temperature fluctuation amplitude at the depth of 2.75–1.70 m. The phase lags corresponded to the maximum values on sinusoidal temperature waves of the two measuring points after filtering and were also used in the calculation of GW velocity as input variables of the analytical model.

The curves representing variation in SW–GW exchange rate during the observation were obtained through the four analytical models described in section "Analytical methods in VFLUX 2". In order to provide a standard, the COMSOL model was used to simulate the seepage law based on the known water head, which was consistent with Naranjo and Smith (2016) research, plus the previous correction of the model temperature, so the COMSOL model was set as a reference. Figure 8 shows the measured head and simulated seepage from the prediction period of March 26, 2012 to November 4, 2012. In addition, the riparian zone vertical seepage velocity was mainly related to head variation as shown in Fig. 8 as they showed the same trend. Figure 9 shows the seepage velocity curves calculated by several different methods. The results obtained by the amplitude (Hatch and Keery), phase (Hatch and Keery) and amplitude-phase combination (McCallum and Luce) methods as well as the COMSOL simulation are illustrated through the curves shown in Fig. 9a–d respectively. The GW velocity near the measuring points showed dynamic fluctuation during the study period and had characteristics as discussed in the following paragraphs.

The velocities at 1.70–2.75 m calculated by the Hatch amplitude and phase methods were 2.47×10^{-6} to 3.15×10^{-6} m/s, and 2.06×10^{-5} to 4.87×10^{-5} m/s, respectively, with the latter approximately ten-fold greater than that of the former. The velocities calculated through the Keery amplitude and phase methods were 2.04×10^{-6} to 2.45×10^{-6} m/s and 2.06×10^{-5} to 4.87×10^{-5} m/s, respectively. Similar to the Hatch solution, the velocities calculated by the Keery solution through the phase method were higher than that calculated through the amplitude method. For the amplitude-phase combination method, the velocity calculated by the McCallum and Luce solutions basically coincided at 1.07×10^{-5} to 3.91×10^{-5} m/s, situated between the amplitude and the phase methods, and similarly the velocities calculated under the phase method were ten-fold greater than those of the amplitude method. As evident in Fig. 9d, the COMSOL simulations differed from the amplitude, phase and amplitude-phase combination method simulations, showing a large fluctuation in velocity. The flow velocity calculated by COMSOL showed a strong fluctuation in velocity coinciding with a strong daily fluctuation in water level with a 1-h sampling frequency. Although data could be measured every hour, the data sampling frequency calculated by VFLUX 2 was 1 every 2 h. The amount of data was relatively small, resulting in a relatively smooth calculated curve. The results of the COMSOL simulation were processed using 5th-order polynomial fitting to allow comparison with the results of VFLUX 2. The fitted velocity was 0.51×10^{-6} to 1.15×10^{-6} m/s.

In general, the results of the amplitude, phase, amplitude-phase combination and COMSOL simulation methods differed in order of magnitude; however, the overall variation in data across the methods showed relative consistency, which further illustrates the reliability of the riparian zone model established by COMSOL. The velocities obtained through the Hatch and Keery phase methods were similar, where those calculated using the Hatch and Keery amplitude methods differed considerably,

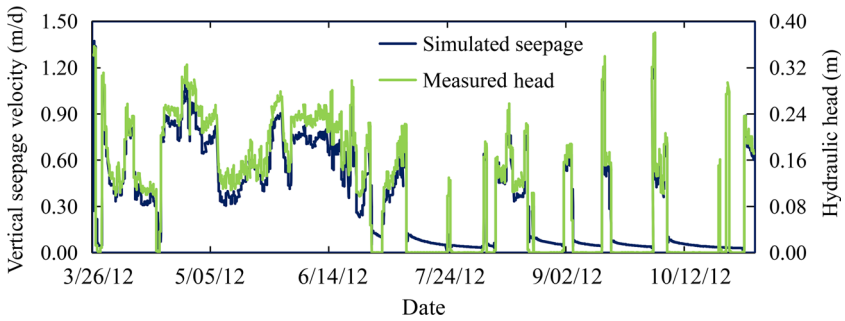

Fig. 8 Measured head and simulated seepage for the March 26, 2012 to November 4, 2012 prediction period

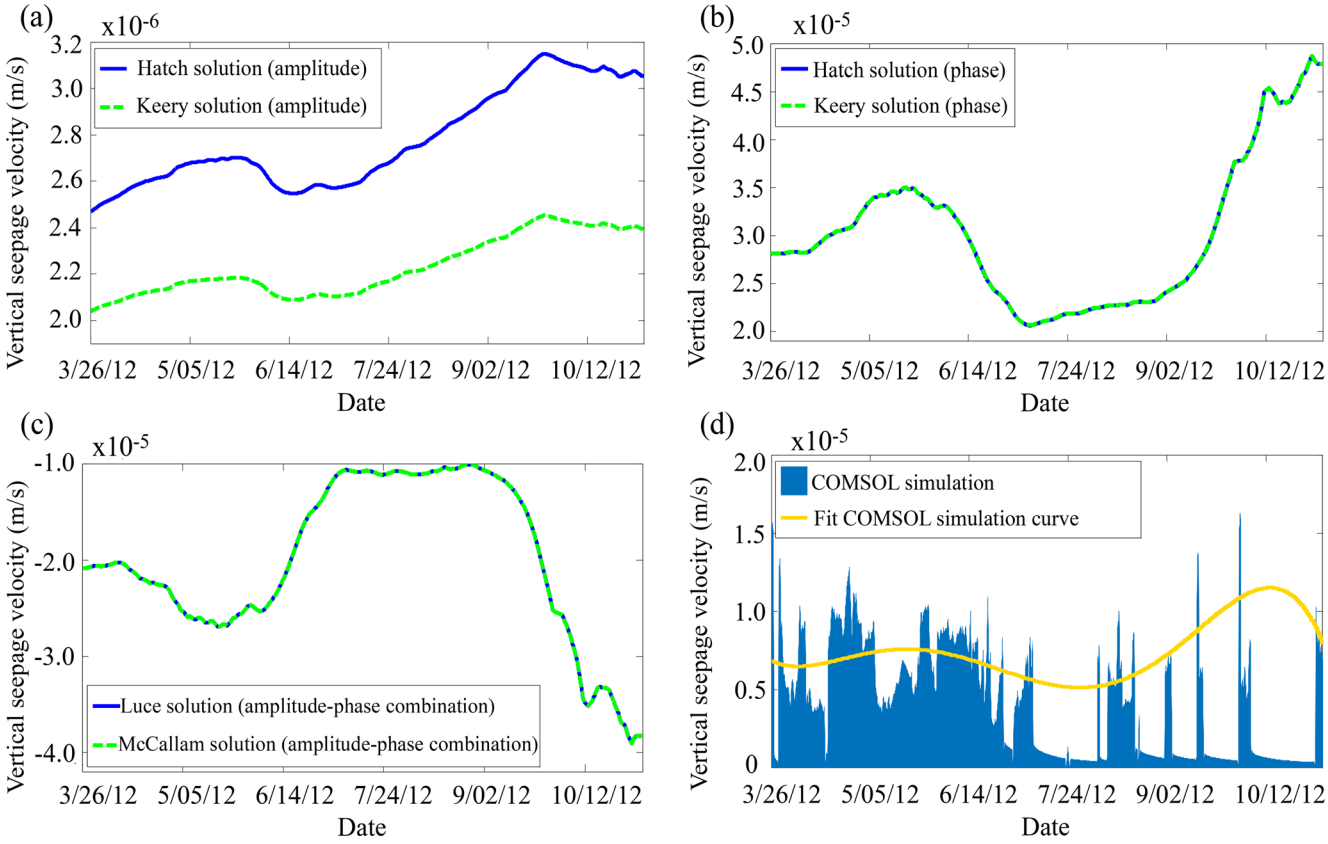

Fig. 9 Velocity curves calculated by different methods. **a** Hatch and Keery solution by the amplitude method; **b** Hatch and Keery solution by the phase method; **c** Luce and McCallam solution by the amplitude-phase combination method; **d** COMSOL simulation method

indicating that the GW velocity computed by the amplitude method was significantly influenced by β under a low velocity. Keery et al. (2007) stressed that the Hatch method offers more accuracy than Keery method due to consideration of the heat dispersion effect.

As is evident in Fig. 9a–d, the velocities calculated by the different analytical solutions differed from that obtained through COMSOL. The Hatch amplitude method and COMSOL simulated velocities were 2.47×10^{-6} to 3.15×10^{-6} m/s and 0.51×10^{-6} to 1.15×10^{-6} m/s, respectively, which were similar in range. However, the velocities calculated through the Hatch phase method and McCallum and Luce amplitude-phase combination methods were different from the COMSOL simulation by an order of nearly 10 in magnitude indicating that GW velocity calculated by the Hatch amplitude method was more accurate. According to the preceding analyses, the Hatch amplitude method was more reliable for the computation of GW velocity; therefore, the Hatch amplitude method was be used in the follow-up analysis of GW velocity.

The GW velocities at different depths of 1.7, 2.3, and 2.75 m through T2, which was 5.8 m from the river center in the horizontal plane, were used in the Hatch amplitude method, denoted by q_1, q_2 and q_3 respectively (Fig. 10). As shown in Fig. 10, the curves of GW velocity at the three depths were approximately parallel and $q_1 > q_2 > q_3$, suggesting that GW velocity decreased with increasing depth. This was mainly because the larger the depth within the saturated zone, the larger the pressure dispersion, and thus the narrower the distribution of GW velocity.

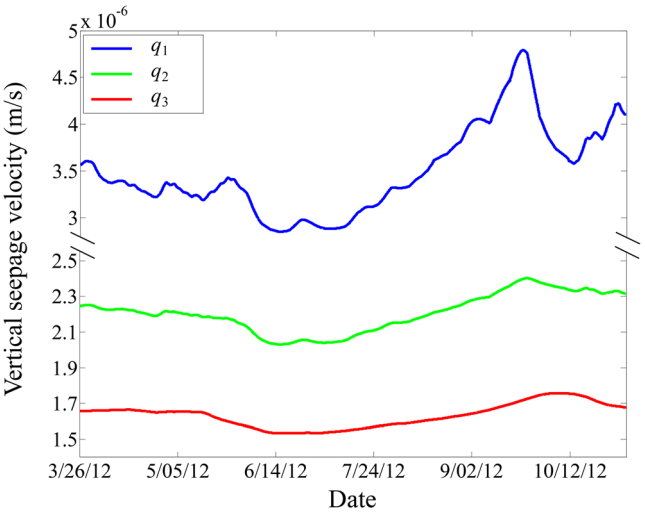

Fig. 10 Curves of vertical seepage velocity at different depths. q_1, q_2 and q_3 represent the vertical seepage velocity at depths of 1.7, 2.3 and 2.75 m below the surface of the riparian zone, respectively

Discussion

The effect of diurnal and seasonal variations on riparian zone temperature

The diurnal variation in water temperature and water level had little influence on riparian zone temperature (Fig. 7 and Table 6). Soil temperature at a depth >1 m is usually insensitive to diurnal cycles of air temperature and solar radiation, whereas the influence of annual air temperature fluctuation extends to a depth of approximately 10 m (Florides and Kalogirou 2005; Anderson 2005). Moreover, Engelhardt et al. (2011) and Lee et al. (2013) found that diurnal temperature fluctuations are not reflected within the deeper hyporheic zone. The depth investigated in the current study ranged from 0.752 to 3.438 m ($-2\ \mathrm{m} \le y \le 0.686\ \mathrm{m}$), which further explained why temperature did not show obvious changes at four different times in spring, summer and winter (Fig. 7 and Table 6).

Compared with three seasonal distributions of temperature shown in Fig. 7, it is obvious that seasonal variation has a significant influence on temperature of the riparian zone, which decreased with sediment depth in spring and summer, but increased in winter. In addition, over the same season, significant variability in riparian sediment temperature occurred in the top layers. This observation is supported by the results of observation during a field survey conducted by Naranjo and Smith (2016) and a previous study by Zhang et al. (2018). The temperature variation can reflect SW–GW exchange (Zhang et al. 2017). As shown in Table 6, the diurnal variations in the patterns and magnitudes of water exchange in the riparian zone were minor compared to seasonal variations.

Since the present study focused on natural rivers, the influence of large-scale hydraulic projects and human factors did not have to be considered; however, dam operations results in large and frequent fluctuations in river stage, which can persist for long distances downstream (Sawyer et al. 2009). Therefore, dam operations fundamentally change the thermal dynamic of riparian aquifers and their hyporheic zones (Wang et al. 2015; Liu et al. 2018), and the variation in temperature for the downstream riparian zone may be dependent on the presence of dams or water projects. Future research should further explore the temporal and spatial distribution of riparian temperature downstream of a dam.

Applicability of different analytical solutions for quantifying hyporheic exchange in the riparian zone

All techniques applied to estimating seepage velocity are prone to errors and uncertainty and all have limitations (Kalbus et al. 2006). Field investigations are usually limited by inadequate instrumentation and low spatial and temporal resolution. High-resolution measurements are required for assessing the spatial heterogeneity and temporal variation of SW–GW interactions. The present study continued the work of previous studies, and determined seepage velocity by temperature time series data (Hatch et al. 2006; Keery et al. 2007; McCallum et al. 2012; Luce et al. 2013). Figure 9 shows that the Hatch solution by amplitude method provided results similar to that of the calibrated model. Although the results of the Hatch and Keery solutions were basically the same, the former takes into account the effect of thermal dispersion, and can therefore theoretically obtain a higher accuracy. As the thermal dispersion was greater than 0.1, the accuracy of Keery solution decreased sharply with increasing thermal dispersion coefficient (Irvine et al. 2015), as also shown in a previous study by Lautz (2012).

Although the Hatch model is accurately able to identify and quantify SW–GW interactions, the results obtained by the amplitude and phase methods were rarely identical (Fig. 9a,b) because the thermophysical parameters related to the porous medium required estimation for the specific applications, and a certain amount of uncertainty was associated with the calculation of the thermophysical parameters, which could readily result in large influences on the aforementioned analytical methods (Shanafield et al. 2011; Rau et al. 2012). To some extent, these factors restrict the ability of these methods to quantitatively describe dynamic process and hyporheic exchange. The McCallum solution uses a combination of the Hatch amplitude equation and the phase equation to derive the amplitude-phase combination method. This method is able to avoid uncertainties in the calculation of the equivalent thermal diffusion coefficient and provides improved applicability in the case of low vertical exchange between SW and GW (McCallum et al. 2012). The Luce solution was approximately expressed by the amplitude ratio of temperature fluctuation signals at two measuring points and the phase lag of temperature fluctuation signals divided by the vertical distance between two measuring points (Luce et al. 2013). Neither the Luce nor Keery analytical solutions considered the effect of thermal dispersion, which can affect the calculation accuracy.

Conclusions

The present study calibrated a 2-D hydro-thermal coupling model using observed temperature and hydraulic head data to quantify hyporheic exchange in the riparian zone. The 2-D heat and flow model was constructed to evaluate the temporal and spatial distribution of temperature in the riparian zone. The calibrated model was used to provide a standard against which to benchmark the performance of four analytical solutions of riparian zone vertical seepage velocity.

The diurnal variations in temperature and water head data showed a minor influence on riparian zone temperature. Diurnal variations in temperature in the riparian unsaturated-saturated zones were approximately consistent and small, with minor water exchange. Seasonal variability had a greater impact on riparian zone temperature, which was mainly expressed as decreases in temperature with increasing sediment depth in spring and summer, but decreases in winter, indicating that the patterns and magnitudes of water exchange in the hyporheic zone varied significantly over different seasons.

Compared with the results of the calibrated hydro-thermal coupling model, the Hatch solution by amplitude method provided more accurate vertical seepage velocity simulations for the study area, estimated to be 2.47×10^{-6} to 3.15×10^{-6} m/s. The vertical seepage velocity of GW gradually increased or decreased over time during the study period, suggesting that riparian SW–GW exchange varied. This exchange can be considered to strengthen or weaken with increasing and decreasing GW velocity over time, respectively. Moreover, the calculated GW velocities were positive, indicating that the riparian zone supplied GW to the river. Longitudinally, the GW velocity near the water level was large, with GW velocity showing a negative relationship with distance to the water level.

Acknowledgements The author is grateful to the US Geological Survey of Reston for sharing data required for this study. We also wish to thank the reviewers for their useful comments and valuable remarks, which significantly improved our manuscript.

Funding information Funding support for this study was provided by National Natural Science Foundation of China (Grant No. 51679194).

Appendix 1: Four analytical solution models for calculating vertical seepage velocity

Hatch solution

The Hatch method identifies analytical solutions for the 1-D heat conduction equation through the temperature fluctuation amplitude ratio of two measuring points and the phase difference (Hatch et al. 2006):

$$v_{z,A_r} = \frac{C}{C_w}\left(\frac{2\kappa_e}{\Delta z}\ln A_r + \sqrt{\frac{\alpha + v_t^2}{2}}\right) \tag{13}$$

$$|v_{z,\Delta\varphi}| = \frac{C}{C_w}\sqrt{\alpha - 2\left(\frac{4\pi\Delta t\kappa_e}{P\Delta z}\right)} \tag{14}$$

where

$$\alpha = \sqrt{v_t^4 + \left(\frac{8\pi\kappa_e}{P}\right)^2}, \qquad \kappa_e = \left(\frac{\lambda_{ts}}{C}\right) + \beta|v_t|,$$
$$\Delta = \frac{P}{2\pi}\left(\varphi_{z+\Delta z,t+\Delta t} - \varphi_{z,t}\right) \approx \frac{P}{2\pi}\left(\varphi_{z+\Delta z,t} - \varphi_{z,t}\right), \quad A_r = \frac{a_{z+\Delta z,t+\Delta t}}{a_{z,t}},$$

and v_{z,A_r} and $|v_{z,\Delta\varphi}|$ are the vertical seepage velocity of the SW infiltrated into the riparian zone calculated by the amplitude method and the phase method, respectively. A negative result indicates the discharge of GW from the riparian zone to the SW. C is the volumetric heat capacity of the saturated sediment and is calculated as the mean of C_w and C_s, where C_w is the specific heat capacity of water, κ_e is the equivalent thermal diffusivity, Δz is the distance between two measuring points, A_r is the ratio of the temperature series curve amplitude of the deep monitoring station A_d to that of the shallow monitoring station A_s, i.e., $A_r = A_d / A_s$, v_t is the velocity of the thermal front, $\Delta\varphi$ is the phase (time) lag between two measuring points, P is period, λ_{ts} is the thermal conductivity of saturated soil, β is the thermal dispersion coefficient, $\varphi_{z,t}$ is phase angle and $a_{z,t}$ is amplitude.

Keery solution

Keery et al. (2007) identified the analytical solution to the Stallman equation (Stallman 1965) which is similar to the Hatch method in form. The Keery solution fails to consider thermal dispersity and is expressed as:

$$\left(\frac{H^3\ln A_r}{4\Delta z}\right)v_{z,A_r}{}^3 - \left(\frac{5H^2\ln^2 A_r}{4\Delta z^2}\right)v_{z,A_r}{}^2 + \left(\frac{2H\ln^3 A_r}{\Delta z^3}\right) + \left(\frac{\pi C}{\lambda_{ts}P}\right) - \frac{\ln^4 A_r}{\Delta z^4} = 0 \tag{15}$$

$$|v_{z,\Delta\varphi}| = \sqrt{\left(\frac{C\Delta z}{\Delta\varphi C_w}\right)^2 - \left(\frac{4\pi\Delta\varphi\lambda_{ts}}{P\Delta z C_w}\right)^2} \tag{16}$$

where $H = \frac{C_w}{\lambda_{ts}}$. By comparing Eqs. (13) and (14) with Eqs. (15) and (16), respectively, it is known that the flow velocity calculated using the phase method has values but no directions.

McCallum solution

Although the Hatch and Keery solutions are more accurately identify and quantify SW–GW interactions, the amplitude and phase methods rarely achieve completely consistent calculations in practical applications. In addition, the thermophysical parameters related to porous media required estimation for specific applications which are uncertain and have a greater impact on the results of the above analytical models (Shanafield et al. 2011; Rau et al. 2012). These factors restrict the application of the preceding analytical models for quantifying the dynamic process and laws of hyporheic exchange.

To solve the aforementioned problems, McCallum et al. (2012) combined the Hatch amplitude equation with the phase equation to obtain the following equations:

$$v_{z,A_r,\Delta\varphi} = -\frac{C}{C_w}\left(\frac{\Delta z\left(P^2\ln^2 A_r - 4\pi^2\Delta\varphi^2\right)}{\Delta\sqrt{16\pi^4\Delta\varphi^4 + 8P^2\pi^2\Delta\varphi^2\ln^2 A_r + P^4\ln^4 A_r}}\right) \quad (17)$$

$$\kappa_e = \frac{\Delta z^2 P^2 \ln A_r\left(4\pi^2\Delta^2 - P^2\ln^2 A_r\right)}{\Delta\left(P^2\ln^2 A_r + 4\pi^2\Delta\varphi^2\right)\left(P^2\ln^2 A_r - 4\pi^2\Delta\varphi^2\right)} \quad (18)$$

where $v_{z,A_r,\Delta\varphi}$ is the vertical seepage velocity calculated by the amplitude-phase combination method.

Luce solution

Luce et al. (2013) conducted a study on the undetermined coefficient scheme of the Stallman analytical solution (Stallman 1965), and obtained the following equations:

$$v_{z,A_r,\Delta\varphi} = \frac{C}{C_w}\left(\frac{\omega\Delta z}{\Delta}\left(\frac{1-\eta^2}{1+\eta^2}\right)\right) = \frac{C}{C_w}\left(\frac{\eta\omega\Delta z}{-\ln A_r}\left(\frac{1-\eta^2}{1+\eta^2}\right)\right) \quad (19)$$

$$\kappa_e = \frac{\omega\Delta z^2}{\Delta\varphi^2\left(\frac{1}{\eta}+1\right)} = \frac{\omega\eta^2\Delta z^2}{\ln^2 A_r\left(\frac{1}{\eta}+1\right)} \quad (20)$$

where $\eta = -\ln A_r/\Delta\varphi$, $\omega = 2\pi/P$.

Appendix 2: The Morris method

The Morris sensitivity analysis method, which was first proposed in 1991 (Morris 1991), is able to effectively identify and rank model parameters according to their importance. Through changing the value of one parameter at a time, the "elementary effect" of each parameter can be calculated in turn, and the impact of input parameters of the model on output data is evaluated. On this basis, the sensitivity level of each parameter and the qualitative description of correlations between parameters are obtained. The Morris sensitivity analysis method is conducted using the following steps: (1) assume that there are k parameters in a numerical model, and each parameter has p sampling points; (2) identify the values of the m parameters on the p sampling points respectively so as to obtain the vector $\mathbf{X} = [x_1, x_2, \cdots, x_k]$; 3) construct $m \times k$ ($m = k + 1$) order matrix $\mathbf{B}$:

$$\mathbf{B} = \begin{bmatrix} 0 & 0 & 0 & 0 & 0 \\ 1 & 0 & 0 & \cdots & 0 \\ 1 & 1 & 0 & \cdots & 0 \\ 1 & 1 & 1 & \cdots & 0 \\ \cdots & \cdots & \cdots & \cdots & \cdots \\ 1 & 1 & 1 & \cdots & 1 \end{bmatrix} \quad (21)$$

The jth column in the matrix $\mathbf{B}$ represents the jth parameter. Values 1 and 0 refer to changed and unchanged parameters, respectively. The differences between calculated values of the parameter combinations in each row represents the global sensitivity when the parameters in the corresponding combination change concurrently.

References

Anderson MP (2005) Heat as a ground water tracer. Groundwater 43(6): 951–968. https://doi.org/10.1111/j.1745-6584.2005.00052.x

Arora B, Spycher NF, Steefel CI, Molin S, Bill M, Conrad ME, Dong WM, Faybishenko B, Tokunaga TK, Wan JM, Williams KH, Yabusaki SB (2016) Influence of hydrological, biogeochemical and temperature transients on subsurface carbon fluxes in a flood plain environment. Biogeochemistry 127(2–3):367–396. https://doi.org/10.1007/s10533-016-0186-8

Boano F, Camporeale C, Revelli R, Ridolfi L (2006) Sinuosity-driven hyporheic exchange in meandering rivers. Geophys Res Lett 33(18): L18406. https://doi.org/10.1029/2006gl027630

Campolongo F, Tarantola S, Saltelli A (1999) Tackling quantitatively large dimensionality problems. Comput Phys Commun 117(1–2): 75–85. https://doi.org/10.1016/S0010-4655(98)00165-9

Cardenas MB (2007) Potential contribution of topography-driven regional groundwater flow to fractal stream chemistry: residence time distribution analysis of Tóth flow. Geophys Res Lett 34(5):L05403. https://doi.org/10.1029/2006gl029126

Cardenas MB (2009) A model for lateral hyporheic flow based on valley slope and channel sinuosity. Water Resour Res 45(1):W01501. https://doi.org/10.1029/2008wr007442

Chen IT, Chang LC, Chang FJ (2017) Exploring the spatio-temporal interrelation between groundwater and surface water by using the self-organizing maps. J Hydrol 556:131–142. https://doi.org/10.1016/j.jhydrol.2017.10.015

Constantz J (2008) Heat as a tracer to determine streambed water exchanges. Water Resour Res 44(4):W00D10. https://doi.org/10.1029/2008wr006996

Cukier RI, Fortuin CM, Shuler KE, Petschek AG, Schaibly JH (1973) Study of the sensitivity of coupled reaction systems to uncertainties in rate coefficients, I: theory. J Chem Phys 59(8):3873–3878. https://doi.org/10.1063/1.1680571

Dwivedi D, Steefel CI, Arora B, Bisht G (2017) Impact of intra-meander hyporheic flow on nitrogen cycling. Procedia Earth Planet Sci 17: 404–407. https://doi.org/10.1016/j.proeps.2016.12.102

Dwivedi D, Steefel CI, Arora B, Newcomer M, Moulton JD, Dafflon B, Faybishenko B, Fox P, Nico P, Spycher N, Carroll R, Williams K (2018a) Geochemical exports to river from the intrameander hyporheic zone under transient hydrologic conditions: East River Mountainous Watershed, Colorado. Water Resour Res 54:8456–8477. https://doi.org/10.1029/2018wr023377

Dwivedi D, Arora B, Steefel CI, Dafflon B, Versteeg R (2018b) Hot spots and hot moments of nitrogen in a riparian corridor. Water Resour Res 54(1):205–222. https://doi.org/10.1002/2017wr022346

Edwardson KJ, Bowden WB, Dahm C, Morrice J (2003) The hydraulic characteristics and geochemistry of hyporheic and parafluvial zones in Arctic tundra streams, north slope, Alaska. Adv Water Resour 26(9):907–923. https://doi.org/10.1016/S0309-1708(03)00078-2

Engelhardt I, Piepenbrink M, Trauth N, Stadler S, Kludt C, Schulz M, Schueth C, Ternes TA (2011) Comparison of tracer methods to quantify hydrodynamic exchange within the hyporheic zone. J Hydrol 400(1–2):255–266. https://doi.org/10.1016/j.jhydrol.2011.01.033

Engelhardt I, Prommer H, Moore C, Schulz M, Schüth C, Ternes TA (2013) Suitability of temperature, hydraulic heads, and acesulfame to quantify wastewater-related fluxes in the hyporheic and riparian zone. Water Resour Res 49(1):426–440. https://doi.org/10.1029/2012wr012604

Florides G, Kalogirou S (2005) Annual ground temperature measurements at various depths. 8th REHVA World Congress Clima, October 9–12, 2005, Lausanne, Switzerland, pp 1–6

Fox A, Boano F, Arnon S (2014) Impact of losing and gaining streamflow conditions on hyporheic exchange fluxes induced by dune-shaped

bed forms. Water Resour Res 50(3):1895–1907. https://doi.org/10.1002/2013wr014668

Fox A, Laube G, Schmidt C, Fleckenstein JH, Arnon S (2016) The effect of losing and gaining flow conditions on hyporheic exchange in heterogeneous streambeds. Water Resour Res 52(9):7460–7477. https://doi.org/10.1002/2016wr018677

Gardner WR, Hillel D, Benyamini Y (1970) Post-irrigation movement of soil water, 1: Redistribution. Water Resour Res 6(3):851–861. https://doi.org/10.1029/wr006i003p00851

Gerecht KE, Cardenas MB, Guswa AJ, Sawyer AH, Nowinski JD, Swanson TE (2011) Dynamics of hyporheic flow and heat transport across a bed-to-bank continuum in a large regulated river. Water Resour Res 47(3):W03524. https://doi.org/10.1029/2010wr009794

Gordon RP, Lautz LK, Briggs MA, McKenzie JM (2012) Automated calculation of vertical pore-water flux from field temperature time series using the VFLUX method and computer program. J Hydrol 420–421:142–158. https://doi.org/10.1016/j.jhydrol.2011.11.053

Goto S, Yamano M, Kinoshita M (2005) Thermal response of sediment with vertical fluid flow to periodic temperature variation at the surface. J Geophys Res 110(B1):B01106. https://doi.org/10.1029/2004jb003419

Hatch CE, Fisher AT, Revenaugh JS, Constantz J, Ruehl C (2006) Quantifying surface water-groundwater interactions using time series analysis of streambed thermal records: method development. Water Resour Res 42(10):W10410. https://doi.org/10.1029/2005wr004787

Healy RW, Ronan AD (1996) Documentation of computer program VS2DH for simulation of energy transport in variably saturated porous media; modification of the US Geological Survey's computer program VS2DT. US Geol Surv Water Resour Invest Rep 96-4230

Hester ET, Guth CR, Scott DT, Jones CN (2016) Vertical surface water-groundwater exchange processes within a headwater floodplain induced by experimental floods. Hydrol Process 30(21):3770–3787. https://doi.org/10.1002/hyp.10884

Hoang L, Griensven AV, Mynett A (2017) Enhancing the SWAT model for simulating denitrification in riparian zones at the river basin scale. Environ Model Softw 93:163–179. https://doi.org/10.1016/j.envsoft.2017.03.017

Huang P, Chui TFM (2018) Empirical equations to predict the characteristics of hyporheic exchange in a pool-riffle sequence. Groundwater 56:947–958. https://doi.org/10.1111/gwat.12641

Ibrakhimov M, Awan UK, George B, Liaqat UW (2018) Understanding surface water-groundwater interactions for managing large irrigation schemes in the multi-country Fergana Valley, Central Asia. Agric Water Manag 201:99–106. https://doi.org/10.1016/j.agwat.2018.01.016

Irvine DJ, Lautz LK, Briggs MA, Gordon RP, Mckenzie JM (2015) Experimental evaluation of the applicability of phase, amplitude, and combined methods to determine water flux and thermal diffusivity from temperature time series using VFLUX 2. J Hydrol 531:728–737. https://doi.org/10.1016/j.jhydrol.2015.10.054

Kalbus E, Reinstorf F, Schirmer M (2006) Measuring methods for groundwater–surface water interactions: a review. Hydrol Earth Syst Sci 10(6):873–887. https://doi.org/10.5194/hess-10-873-2006

Keery J, Binley A, Crook N, Smith JWN (2007) Temporal and spatial variability of groundwater–surface water fluxes: development and application of an analytical method using temperature time series. J Hydrol 336(1–2):1–16. https://doi.org/10.1016/j.jhydrol.2006.12.003

Kiel BA, Cardenas MB (2014) Lateral hyporheic exchange throughout the Mississippi River network. Nat Geosci 7(6):413–417. https://doi.org/10.1038/ngeo2157

Kinal J, Stoneman GL (2012) Disconnection of groundwater from surface water causes a fundamental change in hydrology in a forested catchment in South-Western Australia. J Hydrol 472-473:14–24. https://doi.org/10.1016/j.jhydrol.2012.09.013

Kipp KL (1987) HST3D: a computer code for simulation of heat and solution transport in three-dimensional groundwater flow systems. US Geol Surv Water Resour Invest Rep 86-4095

Lautz LK (2012) Observing temporal patterns of vertical flux through streambed sediments using time-series analysis of temperature records. J Hydrol 464–465:199–215. https://doi.org/10.1016/j.jhydrol.2012.07.006

Lee JY, Lim HS, Yoon HI, Park Y (2013) Stream water and groundwater interaction revealed by temperature monitoring in agricultural areas. Water 5(4):1677–1698. https://doi.org/10.3390/w5041677

Lemke D, Liao ZJ, Wöhling T, Osenbrück K, Cirpka OA (2013) Concurrent conservative and reactive tracer tests in a stream undergoing hyporheic exchange. Water Resour Res 49(5):3024–3037. https://doi.org/10.1002/wrcr.20277

Liao ZJ, Lemke D, Osenbrück K, Cirpka OA (2013) Modeling and inverting reactive stream tracers undergoing two-site sorption and decay in the hyporheic zone. Water Resour Res 49(6):3406–3422. https://doi.org/10.1002/wrcr.20276

Liu YW, Wang W, Hu YM, Cui W (2016) Improving the distributed hydrological model performance in Upper Huai River basin: using streamflow observations to update the basin states via the ensemble Kalman filter. Adv Meteorol 2016:1–14. https://doi.org/10.1155/2016/4921616

Liu DS, Zhao J, Chen XB, Li YY, Weiyan SP, Feng MM (2018) Dynamic processes of hyporheic exchange and temperature distribution in the riparian zone in response to dam-induced water fluctuations. Geosci J 22(3):465–475. https://doi.org/10.1007/s12303-017-0065-x

Lu CP, Chen S, Zhang Y, Su XR, Chen JH (2017) Heat tracing to determine spatial patterns of hyporheic exchange across a river transect. Hydrogeol J 25(6):1633–1646. https://doi.org/10.1007/s10040-017-1553-9

Luce CH, Tonina D, Gariglio F, Applebee R (2013) Solutions for the diurnally forced advection-diffusion equation to estimate bulk fluid velocity and diffusivity in streambeds from temperature time series. Water Resour Res 49(1):488–506. https://doi.org/10.1029/2012wr012380

McCallum AM, Andersen MS, Rau GC, Acworth RI (2012) A 1-D analytical method for estimating surface water–groundwater interactions and effective thermal diffusivity using temperature time series. Water Resour Res 48(11):W11532. https://doi.org/10.1029/2012wr012007

Mckay MD, Beckman RJ, Conover WJ (1979) A comparison of three methods for selecting values of input variables in the analysis of output from a computer code. Technometrics 21(2):239–245. https://doi.org/10.1080/00401706.1979.10489755

Milly PCD (1987) Estimation of Brooks-Corey parameters from water retention data. Water Resour Res 23(6):1085–1089. https://doi.org/10.1029/wr023i006p01085

Molina-Giraldo N, Bayer P, Blum P, Cirpka OA (2011) Propagation of seasonal temperature signals into an aquifer upon bank infiltration. Groundwater 49(4):491–502. https://doi.org/10.1111/j.1745-6584.2010.00745.x

Morris MD (1991) Factorial sampling plans for preliminary computational experiments. Technometrics 33(2):161–174. https://doi.org/10.1080/00401706.1991.10484804

Munz M, Oswald SE, Schmidt C (2016) Analysis of riverbed temperatures to determine the geometry of subsurface water flow around in-stream geomorphological structures. J Hydrol 539:74–87. https://doi.org/10.1016/j.jhydrol.2016.05.012

Munz M, Oswald SE, Schmidt C (2017) Coupled long-term simulation of reach-scale water and heat fluxes across the river–groundwater interface for retrieving hyporheic residence times and temperature dynamics. Water Resour Res 53(11):8900–8924. https://doi.org/10.1002/2017wr020667

Mutiti S, Levy J (2010) Using temperature modeling to investigate the temporal variability of riverbed hydraulic conductivity during storm events. J Hydrol 388(3–4):321–334. https://doi.org/10.1016/j.jhydrol.2010.05.011

Naranjo RC, Smith DW (2016) Quantifying seepage using heat as a tracer in selected irrigation canals, Walker River basin, Nevada, 2012 and 2013. US Geol Surv Sci Invest Rep 2016-5133

O'Toole P, Chambers JM, Bell RW (2018) Understanding the characteristics of riparian zones in low relief, sandy catchments that affect their nutrient removal potential. Agric Ecosyst Environ 258:182–196. https://doi.org/10.1016/j.agee.2018.02.020

Rau GC, Andersen MS, McCallum AM, Acworth RI (2010) Analytical methods that use natural heat as a tracer to quantify surface water–groundwater exchange, evaluated using field temperature records. Hydrogeol J 18(5):1093–1110. https://doi.org/10.1007/s10040-010-0586-0

Rau GC, Andersen MS, Acworth RI (2012) Experimental investigation of the thermal dispersivity term and its significance in the heat transport equation for flow in sediments. Water Resour Res 48(3): W03511. https://doi.org/10.1029/2011wr011038

Ren J, Wang XP, Shen ZZ, Zhao J, Yang J, Ye M, Zhou YJ, Wang ZH (2018) Heat tracer test in a riparian zone: laboratory experiments and numerical modelling. J Hydrol 563:560–575. https://doi.org/10.1016/j.jhydrol.2018.06.030

Richards LA (1931) Capillary conduction of liquids through porous mediums. Physics 1(5):318–333. https://doi.org/10.1063/1.1745010

Saha GC, Li J, Thring RW, Hirshfield F, Paul SS (2017) Temporal dynamics of groundwater-surface water interaction under the effects of climate change: a case study in the Kiskatinaw River watershed, Canada. J Hydrol 551:440–452. https://doi.org/10.1016/j.jhydrol.2017.06.008

Sawyer AH, Cardenas MB, Bomar A, Mackey M (2009) Impact of dam operations on hyporheic exchange in the riparian zone of a regulated river. Hydrol Process 23(15):2129–2137. https://doi.org/10.1002/hyp.7324

Sawyer AH, Cardenas MB, Buttles J (2012) Hyporheic temperature dynamics and heat exchange near channel-spanning logs. Water Resour Res 48(1):W01529. https://doi.org/10.1029/2011wr011200

Schornberg C, Schmidt C, Kalbus E, Fleckenstein JH (2010) Simulating the effects of geologic heterogeneity and transient boundary conditions on streambed temperatures: implications for temperature-based water flux calculations. Adv Water Resour 33(11):1309–1319. https://doi.org/10.1016/j.advwatres.2010.04.007

Shanafield M, Hatch C, Pohll G (2011) Uncertainty in thermal time series analysis estimates of streambed water flux. Water Resour Res 47(3): W03504. https://doi.org/10.1029/2010wr009574

Shao M, Horton R (1998) Integral method for estimating soil hydraulic properties. Soil Sci Soc Am J 62(3):585–592. https://doi.org/10.2136/sssaj1998.03615995006200030005x

Sobol IM (1993) Sensitivity estimates for nonlinear mathematical models. Math Model Comput Exp 1(4):407–414

Stallman RW (1965) Steady one-dimensional fluid flow in a semi-infinite porous medium with sinusoidal surface temperature. J Geophys Res 70(12):2821–2827. https://doi.org/10.1029/jz070i012p02821

Tao P, Wu SH, Dai EF, Liu YJ (2013) Estimating the daily global solar radiation spatial distribution from diurnal temperature ranges over the Tibetan Plateau in China. Appl Energy 107:384–393. https://doi.org/10.1016/j.apenergy.2013.02.053

van Genuchten MT (1980) A closed-form equation for predicting the hydraulic conductivity of unsaturated soils. Soil Sci Soc Am J 44(5):892–898. https://doi.org/10.2136/sssaj1980.03615995004400050002x

Vogt T, Schirmer M, Cirpka OA (2012) Investigating riparian groundwater flow close to a losing river using diurnal temperature oscillations at high vertical resolution. Hydrol Earth Syst Sci 16(2):473–487. https://doi.org/10.5194/hess-16-473-2012

Wang P, Pozdniakov SP, Shestakov VM (2015) Optimum experimental design of a monitoring network for parameter identification at riverbank well fields. J Hydrol 523:531–541. https://doi.org/10.1016/j.jhydrol.2015.02.004

Wang LP, Jiang WW, Song JX, Dou XY, Guo HT, Xu SF, Zhang GT, Wen M, Long YQ, Li Q (2017a) Investigating spatial variability of vertical water fluxes through the streambed in distinctive stream morphologies using temperature and head data. Hydrogeol J 25(5): 1283–1299. https://doi.org/10.1007/S10040-017-1539-7

Wang Y, Ren J, Hu SB, Feng D (2017b) Global sensitivity analysis to assess salt precipitation for CO2 geological storage in deep saline aquifers. Geofluids 2017:1–16. https://doi.org/10.1155/2017/5603923

Wilson AM, Woodward GL, Savidge WB (2016) Using heat as a tracer to estimate the depth of rapid porewater advection below the sediment–water interface. J Hydrol 538:743–753. https://doi.org/10.1016/j.jhydrol.2016.04.047

Yabusaki SB, Wilkins MJ, Fang Y, Williams KH, Arora B, Bargar J, Bargar J, Beller HR, Bouskill NJ, Brodie EL, Christensen JN, Conrad ME, Danczak RE, King E, Soltanian MR, Spaycher NF, Steefel CI, Tokunaga TK, Versteeg R, Waichler SR, Wainwright HM (2017) Water table dynamics and biogeochemical cycling in a shallow, variably-saturated floodplain. Environ Sci Technol 51(6): 3307–3317. https://doi.org/10.1021/acs.est.6b04873

Yao Y, Huang X, Liu J, Zheng C, He X, Liu C (2015) Spatiotemporal variation of river temperature as a predictor of groundwater/surface-water interactions in an arid watershed in China. Hydrogeol J 23(5): 999–1007. https://doi.org/10.1007/s10040-015-1265-y

Young MH, Karagunduz A, Šimůnek J, Pennell KD (2002) A modified upward infiltration method for characterizing soil hydraulic properties. Soil Sci Soc Am J 66(1):57–64. https://doi.org/10.2136/sssaj2002.0057

Zhang JL, Song JX, Long YQ, Zhang Y, Zhang B, Wang YQ, Wang YY (2017) Quantifying the spatial variations of hyporheic water exchange at catchment scale using the thermal method: a case study in the Weihe River, China. Adv Meteorol 2017:1–8. https://doi.org/10.1155/2017/6159325

Zhang JL, Song JX, Long YQ, Kong FH, Wang LP, Zhang Y, Li Q, Wang YQ, Hui YH (2018) Seasonal variability of hyporheic water exchange of the Weihe River in Shaanxi Province, China. Ecol Indic 92:278–287. https://doi.org/10.1016/j.ecolind.2017.06.039